

High Resolution Optical Spectroscopy and Magnetic Properties of Yb^{3+} in Y_2SiO_5

Sacha Welinski,¹ Alban Ferrier,^{1,2} Mikael Afzelius,³ and Philippe Goldner^{1,*}

¹*PSL Research University, Chimie ParisTech, CNRS,*

Institut de Recherche de Chimie Paris, 75005, Paris, France

²*Sorbonne Universités, UPMC Univ Paris 06, Paris 75005, France*

³*Group of Applied Physics, University of Geneva, CH-1211 Geneva 4, Switzerland*

(Dated: June 23, 2016)

Rare earth doped crystals are promising systems for quantum information processing. In particular paramagnetic rare earths could be used to build coherent interfaces with optical and microwave photons. In addition, isotopes with non zero nuclear spins could provide long lived states for quantum state storage and processing. Yb^{3+} is particularly interesting in this respect since it is the only paramagnetic rare earth with a spin 1/2 isotope, which corresponds to the simplest possible level structure. In this paper, we report on the optical and magnetic properties of Yb^{3+} in the two sites of Y_2SiO_5 , a commonly used crystal for quantum applications. We measured optical inhomogeneous linewidths, peak absorption coefficients, oscillator strengths, excited state lifetimes and fluorescence branching ratios. The Zeeman tensors were also determined in the ground and excited states, as well as the ground state hyperfine tensor for the $^{171}\text{Yb}^{3+}$ ($I = 1/2$) isotope. These results suggest that $\text{Yb}^{3+}:\text{Y}_2\text{SiO}_5$ is a promising material for applications like solid state optical and microwave quantum memories.

I. INTRODUCTION

Rare-earth (RE) doped crystals are promising solid state candidates for quantum information processing.¹⁻⁴ In particular, they can show extremely narrow optical homogeneous linewidths at low temperature, in the range of a few kHz to less than 100 Hz.^{5,6} Combined with inhomogeneous linewidths in the GHz range, this allows optical addressing of ions within ensemble for quantum processors, or quantum memories with large time-bandwidth products. Moreover, several RE ions have non-zero nuclear spins, which can act as long-lived, optically addressable qubits.^{7,8} As an example, hyperfine transitions of $\text{Eu}^{3+}:\text{Y}_2\text{SiO}_5$ can show coherence lifetimes (T_2) up to 6 hours at 2 K [9] using various dephasing control techniques, and still reach a few ms at 20 K.¹⁰ Recent results include entanglement storage^{11,12} and light-matter teleportation at the telecom wavelength,¹³ single photon level memories with storage in nuclear spin states,^{14,15} as well as memories with high efficiency,^{16,17} and storage time exceeding one minute.¹⁸ Large and switchable interactions between RE ions have also been observed,¹⁹ as well as single RE detection,^{20,21} which opens the way to quantum processing in these systems.

Paramagnetic RE ions, such as Nd^{3+} or Er^{3+} , have one more degree of freedom due to their electron spins. This can be used to interface microwave photons to a RE doped crystal through a superconducting resonator^{22,23} and obtain quantum memories for superconducting qubits.²⁴⁻²⁶ In this case too, nuclear hyperfine transitions can provide long storage time. We recently showed that $^{145}\text{Nd}^{3+}:\text{Y}_2\text{SiO}_5$ hyperfine transitions have ground state coherence lifetimes up to 9 ms at 5 K, whereas the electron spin T_2 is about 100 μs .²⁷ High fidelity coherent transfer of microwave excitations to nuclear spins was also demonstrated by quantum state tomography. Ultimately, it should be possible to build co-

herent interfaces between optical and/or microwave photonic qubits, and long lived nuclear spin quantum states.

Yb^{3+} ions have attractive properties in this respect. Their $4f^{13}$ configuration comprises only two multiplets: $^2\text{F}_{5/2}$ (ground) and $^2\text{F}_{7/2}$ (excited) separated by ≈ 10000 cm^{-1} . This energy corresponds to the near infrared, where laser diodes are easily found. The excited state decays usually radiatively, with a lifetime of about 1 ms, which sets a limit for the optical coherence lifetime of 2 ms. There are also two naturally abundant isotopes with non-zero nuclear spin: $^{171}\text{Yb}^{3+}$ ($I = 1/2$) and $^{173}\text{Yb}^{3+}$ ($I = 5/2$), which hyperfine transitions could be used as long lived qubits. The lower spin angular momenta of Yb^{3+} compared to Er^{3+} and Nd^{3+} ($I = 7/2$ for all non-zero spin isotopes) result in simpler energy level structures. This is important since optical initialization and coherent manipulation of spins require selecting specific transitions within the optical inhomogeneous linewidth by potentially complex optical pumping sequences. The lower number of spin states in $^{171}\text{Yb}^{3+}$ and $^{173}\text{Yb}^{3+}$ could simplify them considerably.

Here we report on the low temperature and high resolution optical spectroscopy of $\text{Yb}^{3+}:\text{Y}_2\text{SiO}_5$. This crystalline host has been chosen since it shows outstanding properties in terms of narrow optical linewidths and long coherence spin lifetimes when doped with Pr^{3+} , Nd^{3+} , Eu^{3+} and Er^{3+} .^{5,27,28} It is currently the most used host in quantum storage experiments. We measured inhomogeneous linewidths, absorption spectra, excited state lifetimes and branching ratios for the two Yb^{3+} sites and found values among the best for RE doped crystals. Magnetic fields are often used to slow down electron spin relaxation,⁶ which influences optical and spin coherence lifetimes and spectral hole burning efficiency. As a first step towards these dynamical experiments, we determined the ground and excited state g tensors from electron paramagnetic resonance and optical spec-

troscopy. Ground state hyperfine tensors were also found for $^{171}\text{Yb}^{3+}$ and $^{173}\text{Yb}^{3+}$, giving hyperfine structures extrapolated at low magnetic field of a few GHz, suitable for coupling to superconducting resonators. Overall, these results suggest that $\text{Yb}^{3+}:\text{Y}_2\text{SiO}_5$ is suitable to build coherent interfaces with optical and microwave photons, while offering nuclear spin transitions for long lived quantum states.

II. EXPERIMENTAL

We used Y_2SiO_5 (YSO) samples doped at 0.005 at.% (50 ppm) with Yb^{3+} and cut from a boule grown by the Czochralski method. YSO has a monoclinic structure belonging to the C_{2h}^6 (C_2/c) space group. Yb^{3+} can substitute Y^{3+} in two different crystallographic sites, both with a C_1 point symmetry. In addition, non equivalent subsites appear under magnetic fields neither parallel nor perpendicular to b . They are related by the crystal C_2 (b) symmetry axis. Samples were cut along the three principal dielectric axes: b (the C_2 crystallographic axis), D_1 and D_2 . Ytterbium has five stable even isotopes ^{168}Yb , ^{170}Yb , ^{172}Yb , ^{174}Yb and ^{176}Yb with nuclear spin $I=0$ and a total abundance of 69.59%. There are also two odd isotopes, ^{171}Yb , with $I=1/2$ and an abundance of 14.28% and ^{173}Yb with $I=5/2$ and a abundance of 16.13%.

Absorption spectra with 0.1 nm resolution were obtained with a Varian Cary 6000i spectrophotometer. Fluorescence measurements were performed using a Coherent 829 Titanium Sapphire laser pumped by a Coherent Verdi G10 laser, a SpectraPro 750 monochromator (1 nm resolution) and an InGaAs photodiode. Fluorescence lifetimes were measured with a tunable optical parametric oscillator pumped by a Nd:YAG laser (Ekspla NT342B-SH, 6 ns pulse length) as the excitation source, a Jobin-Yvon HR250 monochromator and an InGaAs photodiode. High resolution transmission spectra were recorded by scanning a single mode Toptica DL 100 diode laser (1 MHz linewidth) around 980 nm. Continuous frequency scans of about 15 GHz could be performed. The laser beam was collimated with a power of about 1mW in front of the cryostat. The transmitted signal was detected by a Thorlabs PDA36A photodiode and a reference beam by a Thorlabs PM10A photodiode. A small part of signal was also sent to a Toptica Fabry-Perot Interferometer (1 GHz Free Spectral Range at 980 nm). This allowed us to precisely calibrate the spectra frequency scale. The sample was maintained at 10 K in a CTI-Cryogenics closed-cycle cryostat.

Electron paramagnetic resonance spectra were recorded at 9 K with a Bruker ELEXSYS E500 and an ELEXSYS Super High Sensitivity Probe Head in X-band. For the optical determination of Yb^{3+} excited state g -tensors, the crystal was placed between two permanent NdFeB magnets. The field average value was 217 mT with an inhomogeneity of about 10 % along the laser propagation axis. To record angular variations,

the crystal sat on a pedestal attached to an Attocube ANRv51 stage and was rotated by steps of 10° . The whole assembly was put in a Janis LHe cryostat at 10 K. The transmission spectra were recorded with the set up described above.

III. RESULTS AND DISCUSSION

A. Optical Spectroscopy

1. Absorption and Emission Spectra

We first recorded absorption and emission spectra to determine Yb^{3+} crystal field (CF) level energies. The absorption spectrum (Fig. 1) shows well resolved lines corresponding to transitions from the lowest CF level $^2F_{7/2}(0)$ of the ground multiplet to the three CF levels $^2F_{5/2}(0,1,2)$ of the excited one. These lines are homogeneously broadened except for the two lowest energy ones which are likely to be inhomogeneously broadened.²⁹ A narrow and isolated peak, with a full width at half maximum (FWHM) of 2.8 cm^{-1} , is recorded at 10505 cm^{-1} and corresponds to the $^2F_{7/2}(0)\rightarrow^2F_{5/2}(1)$ transition for site 2. Other transitions above 10300 cm^{-1} are much broader with FWHM between 15 and 25 cm^{-1} . The structures in the range $10450\text{ -}10650\text{ cm}^{-1}$ observed for Yb^{3+} concentrations of a few % [30] are not seen in this 50 ppm doped sample and are therefore attributed to distorted Yb^{3+} sites.

Low doping concentration also prevents energy transfer between sites and allows separate recording of each site's emission spectrum (Fig. 2). These lines correspond to the $^2F_{5/2}(0)\rightarrow^2F_{7/2}(0,1,2,3)$ transitions and, except for the higher energy lines, whose widths are instrument limited, are much broader than those observed in absorption. In addition, many partially resolved lines, that we attribute to vibronic transitions, appear in the range $9760\text{ -}10060\text{ cm}^{-1}$ for site 2. This induces an uncertainty in the $^2F_{7/2}(2)$ level position, which we determined using the strongest peak at 9982 cm^{-1} .

The crystal field levels for both sites are summarized in Table I and are in good agreement with previous studies.^{30,31} CF splittings for the ground and excited multiplets are significantly smaller for site 1, which suggests that it corresponds to the crystallographic site with a coordination number (CN) of 7, in which Y-O distances are larger. Indeed, scalar CF strengths have been found smaller for this site in $\text{Ce}^{3+}:\text{Y}_2\text{SiO}_5$ in a theoretical study.³² In the same way, Pr^{3+} ions with the smaller CF splittings have also a higher absorption coefficient, suggesting a higher relative concentration.³³ Since Pr^{3+} ions have a larger ionic radius than Y^{3+} ones, they should occupy preferentially the CN = 7 site, which has a larger volume.

Because of phonon relaxation between CF levels within the multiplets, only the $0\text{-}0$ ($^2F_{7/2}(0)\text{-}^2F_{5/2}(0)$) transition

TABLE I. Optical transitions in $\text{Yb}^{3+}:\text{Y}_2\text{SiO}_5$. CF level energies; 0-0 transition wavelength (vac.), inhomogeneous linewidths, peak absorption coefficient for different light polarizations, oscillator strength; experimental fluorescence decay time (T_1), spontaneous emission decay time for the 0-0 transition (T_{1s}) and T_{1s}/T_1 ratio.

	Energy (cm^{-1})	λ_{vac} (nm)	Γ_{inh} (GHz)	α_0 (cm^{-1})	$P \times 10^7$	T_1 (ms)	T_{1s} (ms)	T_{1s}/T_1		
	${}^2F_{7/2}$	${}^2F_{5/2}$								
Site 1	0	10189	981.463	2.2	3.3 ($E \parallel D_1$)	5.0	0.87	8.5	9.8	
	111	10391								5.7 ($E \parallel D_2$)
	499	10874								6.5 ($E \parallel b$)
	709									
Site 2	0	10216	978.854	1.7	3.7 ($E \parallel D_1$)	6.4	1.3	6.5	5.0	
	234	10505								10.3 ($E \parallel D_2$)
	612	11076								9.0 ($E \parallel b$)
	970									

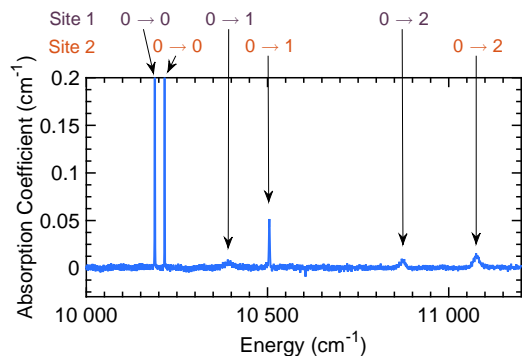


FIG. 1. Unpolarized absorption spectrum of $\text{Yb}^{3+}:\text{Y}_2\text{SiO}_5$ at 12 K with light propagating along the b axis. Transitions between CF levels are indicated for sites 1 and 2.

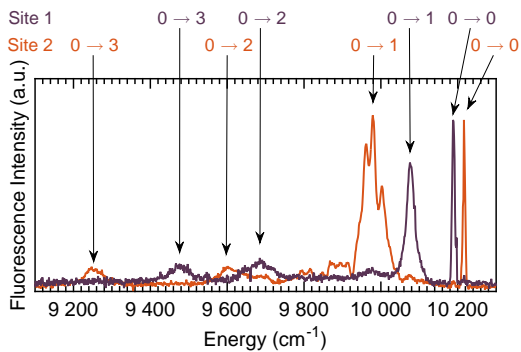


FIG. 2. Emission spectra of sites 1 (purple line) and 2 (orange line) of $\text{Yb}^{3+}:\text{Y}_2\text{SiO}_5$ at 10 K excited respectively at 919 nm and 902 nm. Transitions between CF levels are indicated.

can have a narrow homogeneous linewidth at low temperatures. It is therefore the transition of interest for QIP applications,³ and we focus on it in the following. High resolution absorption spectra for the 0-0 transitions were obtained at zero external magnetic field by scanning a single mode diode laser. Spectra were obtained for the light electric field E polarized along the D_2 and b axes and the wave vector k parallel to D_1 ; for E parallel to D_1 , k was parallel to D_2 (Fig. 3). The lines peak at 10188.87

cm^{-1} (981.463 nm in vac.) and 10216.06 cm^{-1} (978.854 nm in vac.) for sites 1 and 2.

Both lines show a narrow central part, as expected for the $I = 0$ Yb^{3+} isotopes, on top of a broader and weaker structure, in which peaks can be clearly seen in some cases (e.g. site 2, $E \parallel D_2$). We attribute this additional feature to the zero field hyperfine structures of the ${}^{171}\text{Yb}^{3+}$ (abundance 14.3 %) and ${}^{173}\text{Yb}^{3+}$ (abundance 16.1 %) isotopes, which span about 3-4 GHz in the ground state (see Section III B). All lines could be well fitted by a combination of Lorentzian lines (see inset in Fig. 3). This has been observed in several RE doped crystals^{34,35} and, according to Stoneham³⁶, corresponds to perturbations by a low concentration of point defects. The FWHM of the central parts of the lines are 2.2 and 1.7 GHz for sites 1 and 2. These values are comparable to those found for Y_2SiO_5 doped at low levels of RE ions⁵ and are related to the difference in ionic radius between Y^{3+} (0.892 Å) and Yb^{3+} (0.858 Å).³⁷ It is important to note that growth conditions can also have a significant influence on Γ_{inh} [38 and 39].

Large and anisotropic peak absorption coefficients were measured, reaching maximum values of 6.5 cm^{-1} ($E \parallel b$) and 10.3 cm^{-1} ($E \parallel D_2$) for site 1 and 2 respectively. In both cases, the lower absorption occurs for a light electric field polarized along D_1 . The average oscillator strengths P were calculated without local field corrections and assuming equal Yb^{3+} occupancy for the two sites, because of the close ionic radii of Y^{3+} and Yb^{3+} . Site 2 value ($P = 6.4 \times 10^{-7}$) is about 30% higher than the one for site 1 ($P = 5.0 \times 10^{-7}$).

Excited state population lifetimes are around 1 ms for both sites (Table I) and can be considered to be purely radiative. On one hand the low doping concentration prevents energy transfers between Yb^{3+} ions and to quenching centers. On the other hand, the energy gap between the ${}^2F_{7/2}$ and ${}^2F_{5/2}$ multiplets ($\approx 10000 \text{ cm}^{-1}$) is much larger than the Y_2SiO_5 phonon cut-off frequency ($\approx 960 \text{ cm}^{-1}$ [40]) so that multiphonon relaxation is negligible.

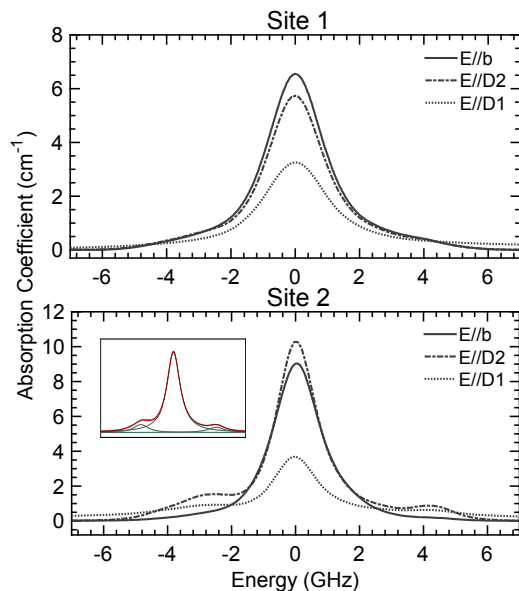


FIG. 3. High resolution absorption spectra of sites 1 (upper graph) and 2 (lower graph) in $\text{Yb}^{3+}:\text{Y}_2\text{SiO}_5$ at 10 K for light electric field polarized along b , D_1 and D_2 axes. Inset: deconvolution of site 2 spectrum for $E \parallel D_2$ by three Lorentzian curves.

2. Comparison with other Rare Earth Ions

In the context of quantum processors and quantum memories, RE with strong optical transitions are needed since they can be coherently driven at a faster rate and result in larger opacity.³ Another important parameter for RE coupled to cavities is the strength of the transition of interest and its relation to all other possible transitions.⁴¹

As the cavity enhances only resonant transitions, achievable emission rates with Purcell enhancement are proportional to the emission rate through the transition that would be coupled to the cavity, 0-0 in our case. The corresponding radiative lifetime T_{1s} is expressed as:

$$(T_{1s})^{-1} = \frac{2\pi e^2 n^2 \nu^2}{\epsilon_0 m c^3} P \quad (1)$$

where e , m are the electron charge and mass, ν is the transition frequency, n the refractive index, c the speed of light, and ϵ_0 the vacuum permittivity. T_{1s} should be as short as possible, with T_1 as a lower bound. On the other hand, decays through uncoupled transitions or non-radiative paths represent a loss for the cavity-emitter system and should be minimized. The ratio T_{1s}/T_1 has therefore to be as small as possible. As showed in Table I, site 2 presents the best values for P , T_{1s} and T_{1s}/T_1 .

Compared to other RE doped crystals investigated for QIP, its oscillator strength is one of the highest reported in the YSO host.^{3,41} It is more than twice the value found in Pr^{3+} , three times that of Er^{3+} and 5 times that of Eu^{3+} . This is mainly due to the 0-0 transition originating from the first excited multiplet and the low J value

of the ground multiplet of Yb^{3+} . Combined with a relatively short and purely radiative T_1 , the reduced number of possible transitions favors a strong 0-0 transition. Still, some RE-host combinations allow larger oscillator strengths, like $\text{Nd}^{3+}:\text{YVO}_4$ (8×10^{-6}) or $\text{Pr}^{3+}:\text{Y}_3\text{Al}_5\text{O}_{12}$ (1.5×10^{-6}).⁴¹

T_{1s} is also short, similar to what is found in $\text{Pr}^{3+}:\text{YSO}$ (5.7 ms) and much shorter than for Er^{3+} (54.6 ms) or Eu^{3+} (120 ms) doped YSO. Compared to systems with very high oscillator strengths, such as $\text{Nd}^{3+}:\text{YVO}_4$, T_{1s} is however about 13 times longer. Finally, T_{1s}/T_1 is very close to the lowest value observed for YSO, 4.8 in $\text{Er}^{3+}:\text{YSO}$ and about one order of magnitude better than for Pr^{3+} (34.5) and Eu^{3+} (63.2). Only $\text{Tm}^{3+}:\text{LiNbO}_3$ shows a significantly lower ratio (2.25). In summary, the 0-0 transition of Yb^{3+} ions in site 2 of YSO shows among the best properties for RE doped crystals in terms of oscillator strength, spontaneous decay T_{1s} and T_{1s}/T_1 ratio.

B. Magnetic Properties

We first determined Yb^{3+} ground state Zeeman and hyperfine tensors by EPR, complementing previous studies where only particular orientations of the magnetic field were investigated.^{31,42} Due to the two crystallographic sites, which generally divide in two sub-sites under a magnetic field, and the two Yb^{3+} isotopes with $I \neq 0$, many lines were observed for magnetic fields B in the range 50-1000 mT. Fig. 4 shows site 1 lines for B at 160° from D_1 in D_1D_2 plane, a configuration where the two subsites, related by a C_2 symmetry along b , are equivalent. Apart from the Zeeman line at 103.5 mT, the two transitions corresponding to $^{171}\text{Yb}^{3+}$ ($I = 1/2$) are observed at 76.1 and 131.2 mT. The other lines located between 64.5 and 144.6 mT are attributed to the hyperfine structure of $^{173}\text{Yb}^{3+}$ ($I = 5/2$). In this case, due to quadrupole interactions, some transitions with $\Delta M_I \neq 0$ are clearly seen. For comparison, the positions of lines corresponding to $\Delta M_I = 0$ and deduced from $^{171}\text{Yb}^{3+}$ hyperfine tensor (see below) are indicated. The lines were very narrow at low magnetic field and FWHMs as low as 12 MHz could be recorded, which is favorable to coupling with high quality factor microwave resonators.²³

The \mathbf{g} tensors of the $I = 0$ isotopes were determined for both sites from angular variations of the Zeeman lines in the three perpendicular planes bD_1 , bD_2 and D_1D_2 (Figs. 5 and S1). All line positions were simultaneously fitted to the Hamiltonian $H = \mu_B \mathbf{B} \cdot \mathbf{g} \cdot \mathbf{S}$, where μ_B is the Bohr magneton and \mathbf{S} is an effective 1/2 spin operator. The C_2 symmetry linking the subsites was also taken into account. The effective spin approach is possible because of the large ground state CF splittings (100 - 200 cm^{-1}) compared to the Zeeman one (0.3 cm^{-1}). Moreover, at low temperature, only the lowest energy CF doublet is populated. For each plane, misalignment between the crystal and the lab frame was also allowed

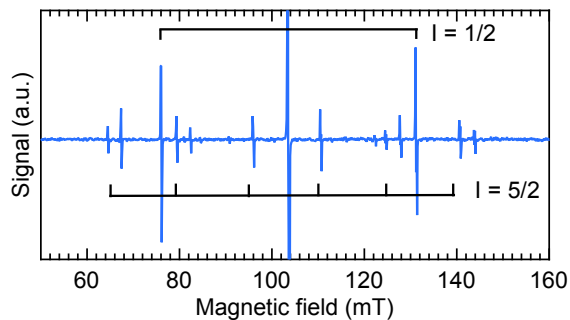


FIG. 4. Site 1 EPR spectrum obtained for B at 160° from D_1 in D_1D_2 plane in $\text{Yb}^{3+}:\text{Y}_2\text{SiO}_5$. Lines corresponding to the $I = 0, 1/2$ and $5/2$ isotopes are observed (see text) and calculated from a spin Hamiltonian model with no quadrupolar contribution.

for by introducing three variable angles in the fit. Excellent agreement with experimental data was obtained, as shown in Figs. 5 and S1. The principal values of \mathbf{g} and the Euler angles for the principal axes are gathered in Table II.

Fig. 6 shows the calculated effective g factors for magnetic fields oriented in the bD_1 , bD_2 and D_1D_2 planes. For site 1, the largest principal value is 6.53, with the principal axis oriented close to the D_1 axis. For site 2, the largest principal value is similar, 6.06, but corresponds to an orientation close to the b axis. This explains the main features of the angular variations of Fig. 5. For both sites, the two other principal values are much smaller. This results in low g factors in the bD_2 and D_1D_2 planes for sites 1 and 2 respectively.

As mentioned above, EPR lines were fitted allowing for crystal misalignment in each plane. For site 1, misalignment angles were below 2° . Surprisingly, these angles were much larger in the case of site 2, reaching for example 7° for the D_1D_2 variation. Moreover, fitting site 1 transitions with site 2 angles resulted in poor agreement with experimental data. This rules out a higher sensitivity of site 2 transitions to crystal misalignment. This discrepancy is particularly clear in the D_1D_2 angular variation (Fig. S1). For magnetic fields around 412 mT (but for different crystal orientations), subsite lines are separated by only 1.2 mT for site 1, whereas site 2 lines are separated by 21.3 mT. This result suggests that the distortion introduced by Yb^{3+} substituting Y^{3+} in site 2 results in an effective C_2 axis direction significantly different from the host crystal. This observation should be further investigated, as it is of importance for predicting particular energy level structures, such as Zero First Order Zeeman shift (ZEFOZ) lines.^{43,44}

The \mathbf{g} tensor of the $^2F_{5/2}(0)$ excited state for the $I = 0$ isotopes was determined using optical measurements, by recording transmission spectra under a magnetic field of about 200 mT. The low 0-0 inhomogeneous linewidth allowed observing four partially resolved transitions in most orientations for both sites. Fig. 7(a) shows a trans-

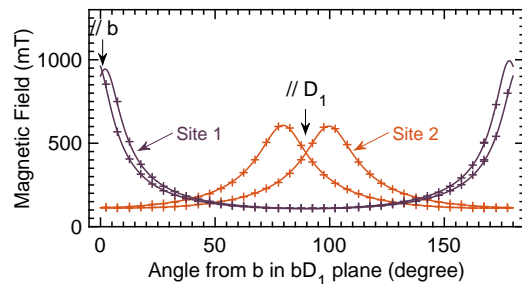


FIG. 5. Angular variation of EPR transitions in the bD_1 plane ($I = 0$ isotopes) for sites 1 and 2 in $\text{Yb}^{3+}:\text{Y}_2\text{SiO}_5$. Crosses: experimental data; lines: fit to a spin Hamiltonian model.

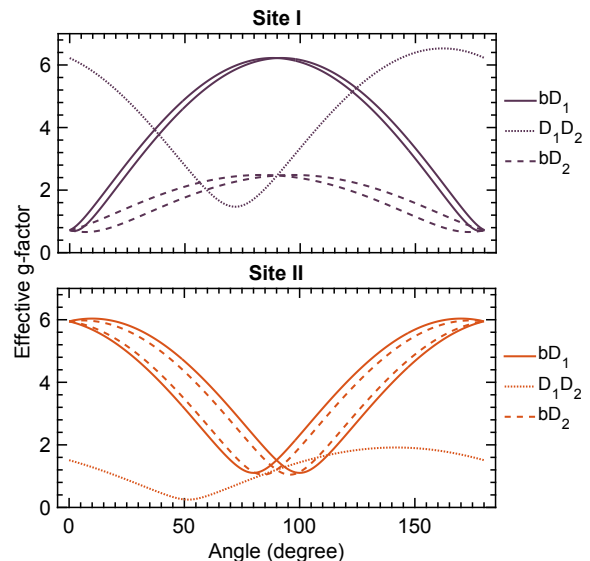


FIG. 6. Calculated effective g factors in the bD_1 , bD_2 and D_1D_2 planes for sites 1 and 2 in $\text{Yb}^{3+}:\text{Y}_2\text{SiO}_5$.

mission spectrum for site 1 with $B \parallel D_2$. In this case, the ground state Zeeman splitting is larger than the excited one and the energy difference corresponding to the effective g factors of the ground and excited states are indicated in Figure 7(a). Effective g factors were determined in the three D_1D_2 , bD_1 and bD_2 planes by rotating the crystal with respect to the magnetic field (Fig. S2 and S3). The values for $B \parallel b$ are in agreement with those reported in [31]. In a first step, the ground state g tensor measured by EPR was compared to the experimental data to check for sample misalignment. The corresponding angles were then used to fit the excited state Zeeman splittings to the spin Hamiltonian in the same way as for the ground state. The calculated effective excited state g factors are shown in Fig. 7(b) and (c).

Table II gives the principal values and axes directions of the excited state g tensors for both sites. The largest values are close, 3.4 and 3.3 for sites 1 and 2, and lower than those of the ground state by a factor of about 2.

This can be qualitatively understood by considering the expression of the g_{zz} component for a pure M_J crystal field level: $g_{zz} = 2g_J M_J$, where g_J is the Landé factor. With $M_J = 7/2$ and $5/2$, we find $g_{zz} = 8$ and 4.3 , which reproduces approximately the experimental ratio of 2. The principal axes corresponding to the largest principal g values are oriented close to the D_1 and b axes for sites 1 and 2. These orientations are close to those obtained for the ground state, which explains that the angular variations and effective g factors in the $D_1 D_2$, bD_1 and bD_2 planes look similar (Figs. 6, 7(b,c), S2 and S3).

It was shown in $\text{Er}^{3+}:\text{YSO}$ that a long optical coherence lifetime could be obtained with strong fields applied in direction where large effective g factors for the ground and excited states are observed in both sites.⁶ At low temperatures, the upper Zeeman levels are strongly depopulated in this configuration, and Er^{3+} spin flips are suppressed. Dephasing of the optical transitions between the lowest Zeeman levels are thus strongly decreased too. In $\text{Er}^{3+}:\text{YSO}$, this could be obtained with a field in the $D_1 D_2$ plane, for which subsites are equivalent. From Figs. 6 and 7, it is clear that a similar strategy in $\text{Yb}^{3+}:\text{YSO}$ requires a magnetic field in the bD_1 plane, which results in magnetically non equivalent subsites and, for example, a reduced optical density. In the $D_1 D_2$ plane or along the b axis, where subsites are magnetically equivalent, one site has always a low effective g factor. Additional experiments are however needed to fully explore this question, as spin dephasing mechanisms may have complex dependences with respect to RE concentration, temperature and magnetic field magnitude and orientation.⁴⁵

We finally determined the ground state hyperfine interaction tensors \mathbf{A} for $^{171}\text{Yb}^{3+}$ ($I = 1/2$) from EPR experiments. The angular variations of the corresponding EPR lines in the $D_1 D_2$, bD_1 and bD_2 planes were fitted to the Hamiltonian:

$$H = \mu_B \mathbf{B} \cdot \mathbf{g} \cdot \mathbf{S} + \mathbf{I} \cdot \mathbf{A} \cdot \mathbf{S}, \quad (2)$$

using the \mathbf{g} tensors and misalignment angles previously determined from the transitions of the $I = 0$ isotopes. Fig. 8(a) shows the angular variation of the two transitions between hyperfine levels in the bD_1 plane for the two subsites of site 2. Experimental data are very well reproduced by the fit, as in the case of the other angular variations (Figs. S4). The principal values and principal axes of \mathbf{A} are given in Table II for sites 1 and 2.

For both sites, the ratio between the tensor elements A_{ij}/g_{ij} is nearly constant for the large A_{ij} and g_{ij} values ($A_{ij}/g_{ij} \approx -0.0264$ for site 1, $A_{ij}/g_{ij} \approx -0.0259$ for site 2), as expected for a pure J multiplet. Indeed, $A_{ij}/g_{ij} = A_J/g_J$ where A_J does not depend on M_J . As a result, the \mathbf{g} and \mathbf{A} tensors of both sites have nearly the same orientation as J mixing by the crystal field should be very small given the large separation between the $^2F_{7/2}$ and $^2F_{5/2}$ multiplets (10000 cm^{-1}) compared to the multiplet splittings ($< 1000 \text{ cm}^{-1}$). The larger deviation between the g and A principal axes orientations for site 2 could

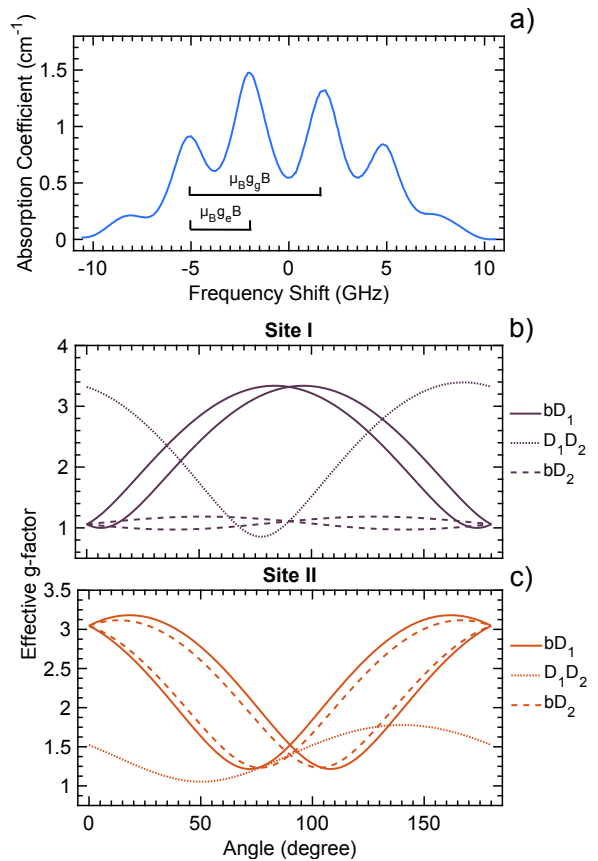


FIG. 7. (a) Transmission spectrum of site 1 in $\text{Yb}^{3+}:\text{Y}_2\text{SiO}_5$ under a magnetic field of 217 mT along the D_2 axis ($T = 10$ K). Energy separations corresponding to the ground and excited state effective g factors are indicated. (b) and (c) calculated excited state effective g factors in the bD_1 , bD_2 and $D_1 D_2$ planes for sites 1 and 2.

be due to an enhanced J mixing effect, consistent with the stronger crystal field of the $\text{CN} = 6$ environment (see Section III A).

The large hyperfine interaction results in zero field splittings of 3.7 and 3.1 GHz for sites 1 and 2, which can be tuned by several GHz using small magnetic fields oriented along the large effective g factors (Fig. 9 for site 1 and S7 for site 2). Moreover, ZEFOZ transitions could appear when the Zeeman and hyperfine interactions start to be comparable. These transitions, also known as clock transitions, are insensitive to magnetic field fluctuations, which can increase their coherence lifetime.^{43,46} A partial ZEFOZ transition is observed around 48 mT in site 1 for a magnetic field oriented along D_2 in Fig. 9. This could be useful for coupling Yb^{3+} ions to superconducting resonators and obtaining quantum memories for microwave photons with long storage time.

We also deduced the hyperfine tensor for $^{173}\text{Yb}^{3+}$ by scaling $^{171}\text{Yb}^{3+}$ \mathbf{A} tensor by the ratio (-0.27) of the nuclear gyromagnetic factors. This accounted for the observed angular variations of $^{173}\text{Yb}^{3+}$ strongest EPR transitions (Fig. 8(b), S5 and S6), although the quadrupole

TABLE II. Magnetic properties of $\text{Yb}^{3+}:\text{Y}_2\text{SiO}_5$. Principal values of the \mathbf{g} and \mathbf{A} ($^{171}\text{Yb}^{3+}$, in MHz) tensors and Euler angles (in degree) defining the principal axis orientations (zxx convention).

	g_x	g_y	g_z	α	β	γ	A_x	A_y	A_z	α_A	β_A	γ_A
Site 1												
Ground state	-0.31	-1.60	6.53	252.8	88.7	113.8	0	-2140	-5302	247	67	122
Excited state	-0.8	1.0	3.4	77	84	173						
Site 2												
Ground state	-0.13	-1.50	6.06	59.1	11.8	347.4	2	1490	-4760	51	11	12
Excited state	-1.0	1.4	-3.3	234	157	190						

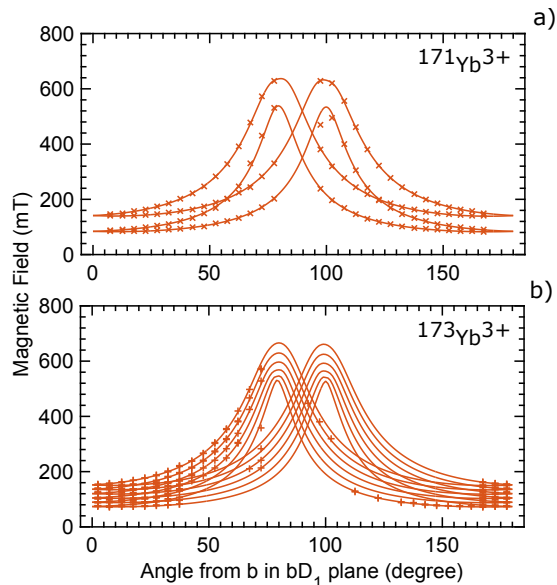


FIG. 8. Angular variations of the EPR transitions of (a) $^{171}\text{Yb}^{3+}$ ($I = 1/2$) and (b) $^{173}\text{Yb}^{3+}$ ($I = 5/2$) in the bD_1 plane in site 2. Crosses: experimental data, lines: fit to a spin Hamiltonian model.

interaction induced small energy shifts and extra $\Delta M_I \neq 0$ transitions (Fig. 4). The calculated zero field splittings are about 3.5 GHz for both sites and show complex behaviors at low fields, including many partial ZEFOZ transitions (Fig. S7). However, this should be taken only as an indication since the quadrupole interaction was not included.

IV. CONCLUSION

Optical properties of a 50 ppm doped $\text{Yb}^{3+}:\text{Y}_2\text{SiO}_5$ crystal have been studied in the context of applications in quantum information processing. In particular, a detailed study of the transition between the lowest crystal field levels of the $^2F_{7/2}$ and $^2F_{5/2}$ multiplets has been carried out at low temperature, allowing the measurements of inhomogeneous broadenings Γ_h , peak absorption coefficients of polarized light, oscillator strengths P , and excited state lifetimes T_1 .

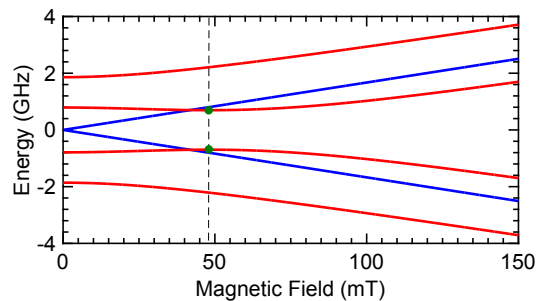


FIG. 9. Calculated energies E of the ground state hyperfine levels of $^{171}\text{Yb}^{3+}$ ($I = 1/2$) in site 1 (red lines) as a function of the magnetic field strength. The field is oriented along D_2 . The vertical dashed line denotes a partial ZEFOZ transition ($dE/dB=0$). The energies of the Zeeman levels of the $I = 0$ isotopes are given for comparison (blue lines).

For Yb^{3+} ions in site 2, we found of $P = 6.4 \times 10^{-7}$, one of the largest value observed for a rare earth ion in Y_2SiO_5 , while $\Gamma_{inh} = 1.7$ GHz. A relatively strong branching ratio was also found for the 0-0 transition, leading to a relaxation rate of $T_{1s} = 6.5$ ms and a ratio $T_{1s}/T_1 = 5.0$. These values also compare favorably with those obtained for other RE doped materials.

We also determined the ground and excited state Zeeman tensors of the $I = 0$ isotopes from angular variations obtained respectively with EPR and optical transmission under a magnetic field of about 200 mT. The largest principal values for both sites are close to $g = 6$ for the ground state and $g = 3$ for the excited state. The corresponding principal axes are close for the ground and excited states and oriented respectively along D_1 and b for sites 1 and 2.

Yb^{3+} is the only paramagnetic rare earth ion with a $I = 1/2$ isotope, which could be advantageous for optical addressing of spin transitions. We therefore determined the ground state A tensor for the $^{171}\text{Yb}^{3+}$ ($I = 1/2$) isotope from EPR measurements. Principal values as large as 5 GHz are observed, leading to calculated total zero field splittings of 3.7 and 3.1 GHz for sites 1 and 2. With magnetic fields oriented along directions of large effective g factors, ground state transitions can be tuned by several GHz with fields of tens of mT. In regions where the Zeeman and hyperfine interactions are

comparable in strengths transitions insensitive to magnetic field fluctuations are predicted, which could lead to increased coherence lifetimes. Extrapolated A tensor for $^{173}\text{Yb}^{3+}$ ($I = 5/2$) isotope is in reasonable agreement with EPR angular variations (Figs. S5 and S6). Calculated zero field splittings are in the same range as for $^{171}\text{Yb}^{3+}$, with a much complex behavior under magnetic field.

In conclusion, these measurements suggest that $\text{Yb}^{3+}:\text{Y}_2\text{SiO}_5$ could be used for quantum information processing with optical, electron and nuclear spin degrees

of freedom.

ACKNOWLEDGMENTS

The authors would like to thank Jean-François Engrand and John G. Bartholomew for their fruitful help. This work received funding from the ANR project DIS-CRYS (No. 14-CE26-0037-01), Idex no. ANR-10-IDEX-0001-02 PSL and Nano-K project RECTUS.

-
- * philippe.goldner@chimie-paristech.fr
- 1 W. Tittel, M. Afzelius, T. Chanelière, R. L. Cone, S. Kröll, S. A. Moiseev, and M. J. Sellars, *Laser & Photon. Rev.* **4**, 244 (2010).
 - 2 C. W. Thiel, T. Böttger, and R. L. Cone, *J. Lumin.* **131**, 353 (2011).
 - 3 P. Goldner, A. Ferrier, and O. Guillot-Noël, in *Handbook on the Physics and Chemistry of Rare Earths*, edited by J.-C. G. Bünzli and V. K. Pecharsky (Elsevier, Amsterdam, 2015) pp. 1–78.
 - 4 M. Afzelius and H. de Riedmatten, in *Engineering the Atom-Photon Interaction*, edited by A. Predojević and M. W. Mitchell (Springer, 2015).
 - 5 R. M. Macfarlane, *J. Lumin.* **100**, 1 (2002).
 - 6 T. Böttger, C. W. Thiel, R. L. Cone, and Y. Sun, *Phys. Rev. B* **79**, 115104 (2009).
 - 7 A. Louchet, Y. Le Du, F. Bretenaker, T. Chanelière, F. Goldfarb, I. Lorget, J.-L. Le Gouët, O. Guillot-Noël, and P. Goldner, *Phys. Rev. B* **77**, 195110 (2008).
 - 8 E. Fraval, M. J. Sellars, and J. J. Longdell, *Phys. Rev. Lett.* **95**, 030506 (2005).
 - 9 M. Zhong, M. P. Hedges, R. L. Ahlefeldt, J. G. Bartholomew, S. E. Beavan, S. M. Wittig, J. J. Longdell, and M. J. Sellars, *Nature* **517**, 177 (2015).
 - 10 A. Arcangeli, R. Macfarlane, A. Ferrier, and P. Goldner, *Phys. Rev. B* **92**, 224401 (2015).
 - 11 C. Clausen, I. Usmani, F. Bussièrès, N. Sangouard, M. Afzelius, H. de Riedmatten, and N. Gisin, *Nature* **469**, 508 (2011).
 - 12 E. Saglamyurek, J. Jin, V. B. Verma, M. D. Shaw, F. Marsili, S. W. Nam, D. Oblak, and W. Tittel, *Nat. Photonics* **9**, 83 (2015).
 - 13 F. Bussièrès, C. Clausen, A. Tiranov, B. Korzh, V. B. Verma, S. W. Nam, F. Marsili, A. Ferrier, P. Goldner, H. Herrmann, C. Silberhorn, W. Sohler, M. Afzelius, and N. Gisin, *Nat. Photonics* **8**, 775 (2014).
 - 14 P. Jobez, C. Laplane, N. Timoney, N. Gisin, A. Ferrier, P. Goldner, and M. Afzelius, *Phys. Rev. Lett.* **114**, 230502 (2015).
 - 15 M. Gündoğan, P. M. Ledingham, K. Kutluer, M. Mazzera, and H. de Riedmatten, *Phys. Rev. Lett.* **114**, 230501 (2015).
 - 16 M. P. Hedges, J. J. Longdell, Y. Li, and M. J. Sellars, *Nature* **465**, 1052 (2010).
 - 17 J. Dajczgewand, J.-L. Le Gouët, A. Louchet-Chauvet, and T. Chanelière, *Opt. Lett.* **39**, 2711 (2014).
 - 18 G. Heinze, C. Hubrich, and T. Halfmann, *Phys. Rev. Lett.* **111**, 033601 (2013).
 - 19 R. Ahlefeldt, D. L. McAuslan, J. J. Longdell, N. B. Manson, and M. J. Sellars, *Phys. Rev. Lett.* **111**, 240501 (2013).
 - 20 R. Kolesov, K. Xia, R. Reuter, R. Stöhr, A. Zappe, J. Meijer, P. R. Hemmer, and J. Wrachtrup, *Nat. Commun.* **3**, 1029 (2012).
 - 21 T. Utikal, E. Eichhammer, L. Petersen, A. Renn, S. Götzinger, and V. Sandoghdar, *Nat. Commun.* **5**, 3627 (2014).
 - 22 M. U. Staudt, I.-C. Hoi, P. Krantz, M. Sandberg, M. Simoen, P. Bushev, N. Sangouard, M. Afzelius, V. S. Shumeiko, G. Johansson, P. Delsing, and C. M. Wilson, *J. Phys. B: At. Mol. Opt. Phys.* **45**, 124019 (2012).
 - 23 S. Probst, H. Rotzinger, S. Wünsch, P. Jung, M. Jerger, M. Siegel, A. V. Ustinov, and P. A. Bushev, *Phys. Rev. Lett.* **110**, 157001 (2013).
 - 24 M. Afzelius, N. Sangouard, G. Johansson, M. U. Staudt, and C. M. Wilson, *New J. Phys.* **15**, 065008 (2013).
 - 25 S. Probst, H. Rotzinger, A. V. Ustinov, and P. A. Bushev, *Phys. Rev. B* **92**, 014421 (2015).
 - 26 A. Arcangeli, A. Ferrier, and P. Goldner, *Phys. Rev. A* **93**, 062303 (2016).
 - 27 G. Wolfowicz, H. Maier-Flaig, R. Marino, A. Ferrier, H. Vezin, J. J. L. Morton, and P. Goldner, *Phys. Rev. Lett.* **114**, 170503 (2015).
 - 28 I. Usmani, M. Afzelius, H. de Riedmatten, and N. Gisin, *Nat. Commun.* **1**, 12 (2010).
 - 29 Z. Kis, G. Mandula, K. Lengyel, I. Hajdara, L. Kovacs, and M. Imlau, *Opt. Mat.* **37**, 845 (2014).
 - 30 R. Gaumé, P. H. Haumesser, B. Viana, D. Vivien, B. Ferland, and G. Aka, *Opt. Mat.* **19**, 81 (2002).
 - 31 A. Denoyer, Y. Lévesque, S. Jandl, O. Guillot-Noël, P. Goldner, B. Viana, F. Thibault, and D. Pelenc, *J. Phys.: Condens. Matter* **20**, 125227 (2008).
 - 32 J. Wen, C.-k. Duan, L. Ning, Y. Huang, S. Zhan, J. Zhang, and M. Yin, *J. Phys. Chem. A* **118**, 4988 (2014).
 - 33 R. W. Equall, R. L. Cone, and R. M. Macfarlane, *Phys. Rev. B* **52**, 3963 (1995).
 - 34 F. Könz, Y. Sun, C. W. Thiel, R. L. Cone, R. Equall, R. Hutcherson, and R. M. Macfarlane, *Phys. Rev. B* **68**, 085109 (2003).
 - 35 F. Beaudoux, O. Guillot-Noël, J. Lejay, A. Ferrier, and P. Goldner, *J. Phys. B: At. Mol. Opt. Phys.* **45**, 124014 (2012).
 - 36 A. M. Stoneham, *Rev. Mod. Phys.* **41**, 82 (1969).
 - 37 R. D. Shannon and C. T. Prewitt, *Acta Cryst. B* **25**, 925

- (1969).
- ³⁸ A. Ferrier, B. Tumino, and P. Goldner, *J. Lumin.* **170**, 406 (2016).
- ³⁹ T. Böttger, Y. Sun, C. W. Thiel, and R. L. Cone, *Phys. Rev. B* **74**, 075107 (2006).
- ⁴⁰ S. Campos, A. Denoyer, S. Jandl, B. Viana, D. Vivien, P. Loiseau, and B. Ferrand, *J. Phys.: Condens. Matter* **16**, 4579 (2004).
- ⁴¹ D. L. McAuslan, J. J. Longdell, and M. J. Sellars, *Phys. Rev. A* **80**, 062307 (2009).
- ⁴² I. N. Kurkin and K. P. Chernov, *Physica B* **101**, 233 (1980).
- ⁴³ E. Fraval, M. J. Sellars, and J. J. Longdell, *Phys. Rev. Lett.* **92**, 077601 (2004).
- ⁴⁴ D. L. McAuslan, J. Bartholomew, M. J. Sellars, and J. J. Longdell, *Phys. Rev. A* **85**, 032339 (2012).
- ⁴⁵ T. Böttger, C. W. Thiel, Y. Sun, and R. L. Cone, *Phys. Rev. B* **73**, 075101 (2006).
- ⁴⁶ G. Wolfowicz, A. M. Tyryshkin, R. E. George, H. Riemann, N. V. Abrosimov, P. Becker, H.-J. Pohl, M. L. W. Thewalt, S. A. Lyon, and J. J. L. Morton, *Nat. Nanotechnol.* **8**, 561 (2013).